Behavior of Half-Joints: Design and Simulation of Laboratory Tests

Chemical Engineering Journal 499 (2024) 156189

Contents lists available at ScienceDirect

Chemical Engineering Journal

journal homepage: www.elsevier.com/locate/cej

Unlocking enhanced piezoelectric performance through 3D printing of particle-free ceramic piezoelectric complex structures and metamaterials

Tamar Rosental [a,1], Gabriele Gatani [b], Candido Fabrizio Pirri [b], Carlo Ricciardi [b], Daria Savraeva [a], Ayelet Bunin [a], May Yam Moshkovitz-Douvdevany [a], Shlomo Magdassi [a,*], Stefano Stassi [b,*,1]

[a] Casali Center for Applied Chemistry, Institute of Chemistry, The Hebrew University of Jerusalem, Jerusalem 91904, Israel
[b] Department of Applied Science and Technology, Politecnico di Torino, Corso Duca Degli Abruzzi, 24, 10129 Torino, Italy

ARTICLE INFO

Keywords:
3D printing
Piezoelectric
Barium titanate
Metamaterial
Sensors

ABSTRACT

Piezoelectric materials have found widespread use in miniaturized sensors and actuators due to their ability of mutual conversion of mechanical and electric energy. However, current fabrication techniques for these materials are limited to either bulky structures or thin films, restricting the potential that could arise from developing devices with more intricate geometries. Here, we have developed particle-free piezoelectric ink and successfully employed in 3D printing complex barium titanate (BTO) devices using Digital Light Processing technology. The sol–gel process overcomes the viscosity and light scattering issues associated with the slurry traditionally used in 3D printing of piezoelectric ceramic materials. Printed BTO exhibits a remarkable piezoelectric coefficient of 50 pm/V and is utilized to create 3D micrometric structures for applications as both active devices, such as actuators, and passive devices, including displacement sensors and energy harvesters. Furthermore, the flexibility in device fabrication enabled us to 3D print metamaterial piezoelectric structures, designed to concentrate mechanical stress, thereby enhancing the electrical response compared to conventional bulk structures. This research not only advances the field by overcoming fabrication challenges but also opens avenues for creating innovative devices. The design freedom afforded by additive manufacturing technology further underscores the potential for groundbreaking developments in this domain.

1. Introduction

Piezoelectric materials are characterized by a direct link between mechanical and electrical domain. A mutual conversion of mechanical and electric energy is possible is the presence of an asymmetry in the material crystal structure. This asymmetry creates dipoles made of opposite electric charges in each crystal. Under a mechanical stress, these dipoles generate a charge unbalance in opposite face of the material, inducing an electrical voltage. Vice versa, the application of an electric field tends to move the crystal charges causing a mechanical deformation of the material. Both direct and converse piezoelectric effect has been determined a widespread exploitation of these materials in applications such as ultrasonic generation and sensing [1,2], energy harvesting [3–6], strain sensing [7,8] and mechanical actuation [9,10].

Because of the wide numbers of possible applications, several fabrication methods of piezoelectric materials have been investigated. Piezoelectric ceramics are mostly fabricated by injection molding, casting and dice-and-fill techniques [11–13]. These methods are highly effective to obtain device with excellent piezoelectric properties, but are limited to the preparation of bulky structures and unsuitable to fabricate complex shapes or microstructures. More flexibility in design and fabrication could be obtained with piezoelectric polymer, mainly polyvinylidene difluoride (PVDF) and its derivate, that could be processed by solution casting, electrospinning, extrusion and dip-coating [14–16]. However, piezoelectric polymers are widely investigated in research field, but their industrial implementation is negligible because of the intrinsic much lower piezoelectric coefficient with respect of their ceramic counterparts.

In recent time, the development of additive manufacturing technologies opened the possibility to craft three-dimensional (3D) structures

* Corresponding authors.
E-mail addresses: shlomo.magdassi@mail.huji.ac.il (S. Magdassi), stefano.stassi@polito.it (S. Stassi).
[1] These authors equally contributed to this work.

https://doi.org/10.1016/j.cej.2024.156189
Received 15 May 2024; Received in revised form 13 September 2024; Accepted 25 September 2024
Available online 27 September 2024

characterized by intricate geometry [17–19]. Most common 3D printing technologies, such as fused deposition modeling (FDM) [20,21], direct ink writing (DIW) [22,23], selective laser sintering (SLS) [24], and stereolithography, have been optimized to print also ceramic materials, thus overcome the planar limitation in the development of piezoelectric devices expanding the diverse possible applications. Among the various 3D printing technologies available, Vat polymerization (VP) techniques like stereolithography (SLA) [25,26] and digital light processing (DLP) [27,28] are most popular for the 3D printing of high-resolution and high-precision ceramic objects. VP processes require a fluid material (photoresin) that can undergo localized photo-polymerization using a suitable light source and patterned light exposure. In the case of ceramic objects, the printing composition typically contains ceramic particles dispersed within an organic photoresin. A representative example of the advantages of 3D printing technology in the piezoelectric field was illustrated by Cui et al. [29]. In their work, a slurry of lead zirconate titanate (PZT) nanoparticles and photosentitive polymer was prepared and optimized for fabricating objects by a high-resolution projection stereolithography printing. Thanks to additive manufacturing, three-dimensional (3D) building blocks with designed and assembled to obtain inaccessible classes of piezoelectric materials that have arbitrary piezoelectric coefficient tensors. Piezoelectric metamaterials made of organic matrix with embedded PZT particles were fabricated to reach a variety of functions, including force magnitude and directionality detection, and self-monitoring structures, with three-dimensional pressure location mapping.

However, this micro and nanoparticle-based approach has some drawbacks. The compositions are often too viscous to recoat the vat film during printing and often require specialized printers, flocculation and sedimentation of particles is often encountered. In addition, there are severe light scattering which interferes with the photo-polymerization reaction, resulting in reduced spatial resolution. To achieve a ceramic object rather than polymers embedded with ceramic particles, the process requires a thermal step after printing which remove the polymer matrix and sinter the ceramic particles, which tends to result into a porous polycrystalline structures with several not homogenous area. Moreover, this approach may not be suitable for printing dispersions with ceramic materials having a high refractive index, such as barium titanate ($BaTiO_3$ or BTO), nowadays representing one of the most common and highly performing lead-free piezoelectric alternative to PZT, which employment needs to be reduced following the international regulation on lead utilization reduction. The high refractive index causes a decrease in the penetration depth of the UV light. The shallow penetration depth decreases the possible layers thickness and forcing a prolonged printing duration. Liu at el. Reported recently on achieving ten times faster printing, 60 μm s^{-1},using a new technology, continuous liquid inter- face production (CLIP) [30]. The current work presents a higher printing speed of up to 80 μm s^{-1} using the common DLP technology, that is enabled by the much lower light scattering. In recent years, we have developed particle-free inks based on sol–gel processes that overcome the obstacles with particles-based inks since the resin used in the printing process is entirely in liquid phase [31,32]. Sol-gel processes are based on chemical reaction that involves the polymerization of small metal precursors to form a metal-oxide network. By adding UV-polymerizable monomers and proper photoinitiators, these inorganic polymers can be printed by localized light activation. These monomers form bonds with the inorganic polymers, producing hybrid UV-curable inks that are transparent and highly reactive to UV irradiation. The as-printed structures are composed of amorphous gel, which is converted to ceramic objects upon proper post printing processes.

Here we developed a piezoelectric particle-free printing compositions based on sol–gel processes that can be successfully used to 3D print barium titanate complex structures with Digital Light Processing technology performed with low cost printers. Upon thermal treatment, highly dense, fully ceramic, homogenous structures are obtained with a remarkable piezoelectric coefficient of 50 pm/V. The potentiality of 3D printing particle-free piezoelectric device is demonstrated by fabricating piezoelectric Micro-Electro Mechanical Systems (MEMS) devices and validating their applications as sensors, actuators and energy harvesting devices. The complex structuration that can be obtained by 3D printing technology has also been used to increase the piezoelectric performance by fabricating a metamaterial piezoelectric devices which shows a four fold electrical generation enhancement with respect of a bulk counterpart.

2. Results

2.1. Printing, post-printing, and material characterization

In this study, we used a combination of a sol–gel process for obtaining BTO, with a photo-polymerization process. We employed barium acetate salt and titanium alkoxide as $BaTiO_3$ sol–gel precursors, acrylic acid, and Trimethylolpropane Triacrylate (TMPTA) as the photopolymerizable components. A high fraction of sol–gel composition was necessary to later achieve a dense ceramic body. We addressed this issue by adding acetic acid to control gelation by forming multidentate bonds with the metal ions. This enables a higher concentration of the sol–gel components and prolonged the time until spontaneous gelation occurs to days (in contrast to localized UV induces polymerization during the printing). Acrylic acid, which can chelate metal ions, formed hybrid photopolymerizable oligomers with $BaTiO_3$ sol. The resulting composition have low viscosity and is UV reactive [32]. A desktop DLP printer was used to print gel objects composed of an amorphous BTO matrix. The XY resolution was evaluated by printing rectangles (5×5 mm^2) and comparing their dimensions to the corresponding CAD file. This assessment involved measuring the area of each printed rectangle using ImageJ software. Fig. S1 shows the resolution in % as a function of the energy dosage, which is the product of light intensity, given in units of mW/cm^2, and the exposure time in seconds. The resolution refers to the ratio between the printed and designed areas, expressed as a percentage. Optimal resolution denotes a 100 % correlation between the designed object and the resultant printed object, graphically represented by the black line. A ratio exceeding 100 % indicates an over-curing state, while a ratio below 100 % indicates under-curing state. As anticipated, higher energy dosage increases the printed area relative to the designed area. An energy dose of 90 mJ/cm^2 was found to be required for optimal-resolution printing. This energy can be converted to printing parameters of 15 mJ/cm^2 light intensity with a 6-second exposure time. The resolution enabled by this composition was studied. Using the exposure for 3 s at power of ~23 mW/cm^2 parameters, a minimum polymerizable bar widths and spacings test was conducted using an STL file containing a series of bars and gaps ranging from 100 μm to 1 mm. Fig. S2 shows that the minimum bar width that could be printed is 200 μm thick, and the minimum gap between bars is 50 μm.The gel objects required two weeks of slow evaporation of the volatile compounds. During this period a linear shrinkage of about 30 % was observed and reported in a previous paper [32], and the gel objects retain their shape without cracks formation. After two weeks the objects are heated to high temperatures, in which the organic part is decomposed, and the amorphous matrix crystallizes and sinters to form a BTO-dense objects. As seen in Fig. 1, there is a slight un-even shrinkage and deformation of the printed object. This may result from the attachment of the printed object onto the printing substrate, which had different thermal expansion. This can be addressed by printing additional thin “raft-supports” that can be easily removed after sintering. During the whole process, a 60 % linear homogenous shrinkage is observed and the resulting objects retain their printed shape (40 % of printed dimensions) and are composed of 98 % of the theoretical density, as studied previously [32]. The sintering conditions enabling achieving this density were heat treatment at 1430 °C for one hour. The high density is achieved due to the very low concentration of organic monomers required for solidification during printing, and due to the long aging process that is followed by sintering at high

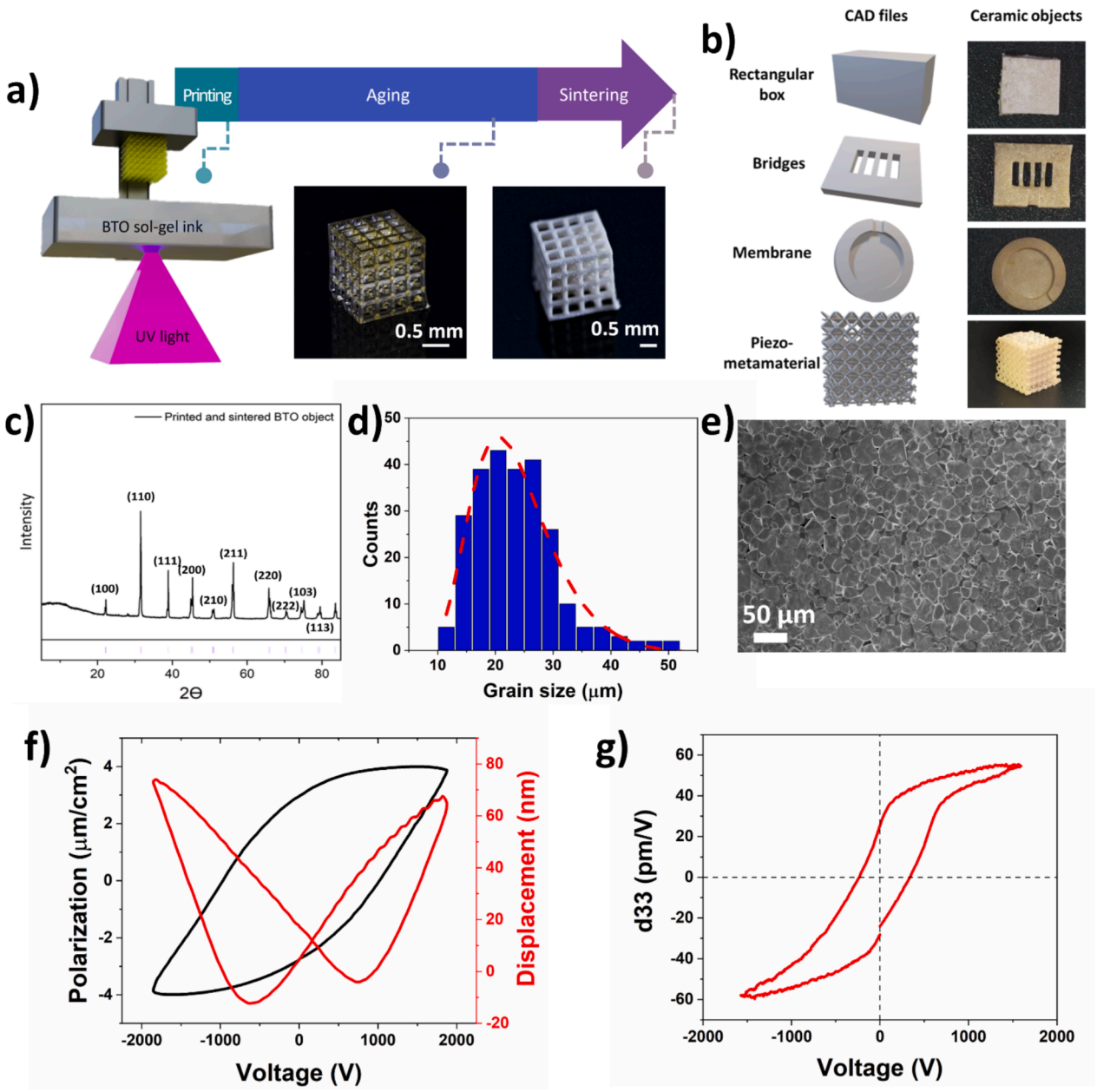

Fig. 1. a) Schematic presentation of the overall fabrication process of BTO. after DLP printing, the gel objects are aged and then sintered. scale bars corresponds to 0.5 mm. b) CAD files and photos of achieved ceramic objects of the four designs that were printed to evaluate the piezoelectric properties and functioning. c) XRD pattern of a printed object after sintering at 1430 °C. d) Grain size dispersion computed over a sample of planar printed barium titanate reported in SEM figure e). Scale bars corresponds to 50 μm. f) Ferroelectric polarization hysteresis (black) loop, displacement butterfly loop (red) and g) d_{33} curve loops of 3D printed bulk barium titanate. (For interpretation of the references to colour in this figure legend, the reader is referred to the web version of this article.)

temperature. The overall process is schematically presented in Fig. 1a.

After developing the composition and the post-printing processes, we obtained printed objects composed of dense BTO. The X-Ray Diffraction (XRD) pattern, shown in Fig. 1c, reveals that the ceramic object is composed of crystalline $BaTiO_3$ only, in it's tetragonal phase. In XRD pattern, the splitting of the (2 0 0) peak at 45° is caused by the off-centering of Ti^{4+} ions, related to a tetragonal non-centrosymmetric phase in the barium titanate crystal which gives it a permanent electric dipole [33]. Also Energy-Dispersive X-ray (EDX) Spectroscopy (Fig. S3) confirm the presence of only barium titanate without any organic materials. After thermal treatment, barium titanate crystallize in grains of different size to completely cover the geometry (Fig. 1d and e). Grain size was estimated from Scanning Electron Microscopy (SEM) analysis to range from 15 μm up to 55 μm with an average value around 23 μm, as shown by the analysis of Figure d. For evaluation of the piezoelectric performance, four types of objects were printed. The relevant CAD files and the resulting structures are presented in Fig. 1b. Full bulk structure to evaluate the piezoelectric characteristic of the printed barium titanate, clamped–clamped beams (bridges) and membranes to demonstrate the application of 3D printed piezoelectric devices as sensors, harvesters and actuators and a Cellular piezo-metamaterial that is expected to enhance the piezoelectric properties [29,34], underlying the potentiality of the printing technology in piezoelectric field.

2.2. Piezoelectric characterization

Ceramic samples prepared by 3D printing approach were

characterized by a Piezoelectric Evaluation System (PES) to extract the piezoelectric figures of merit of the materials. The technique is based on the inverse piezoelectric effect, measuring the mechanical displacement of the material under the application of an electric field. Typical ferroelectric polarization hysteresis and displacement curve (Fig. 1f) were obtained on BTO printed samples (rectangular bulk sample 3 mm wide, 3 mm long and 1 mm thick), as expected since the material present both ferroelectricity and piezoelectricity. From the displacement "butterfly" curve, piezoelectric constant d_{33} were obtained from the slope of the linear part of the plot, as evidenced in Fig. 1f where a d_{33} value of 42 pm/V is reported from a printed Barium Titanate bulk sample. More reliable values of d33 coefficient are obtained by small-signal characterization. In this case, piezoelectric coefficient can be extracted from the saturation values of d_{33}-loop (Fig. 1g) obtained by exciting piezoelectric sample with a sinusoidal high frequency low voltage signal superimposed to a triangular low frequency high voltage one [35]. From the presented graph a value of d_{33} of 51 pm/V can be extracted. To strengthen our investigation, five different samples have been tested obtaining a mean d_{33} value of 50 pm/V $\pm$ 8 pm/V. The obtained value is lower than piezoelectric coefficient of a bulk crystalline sample (242 pm/V, see Fig. S4), but it is in line with literature examples of 3D printed lead-free piezoelectric materials [36]. Few examples with higher piezoelectric constant for $BaTiO_3$ 3D printed materials has been published, but they are all obtained by printing a slurry composed of polymeric matrix with embedded ceramic micro/nanoparticles [25,37]. The printed slurry is then thermally cured to remove the organic matrix and sintering the ceramic particles, resulting into a porous polycrystalline structures with several not homogenous area. Higher values also were achieved by using specialized SLA printer that continuously mixing the slurry in the vat to prevent sedimentation [38]. On the counterpart our approach which is based on a particle-free resin and on the crystallization of a metal–organic precursor, allows the fabrication of highly dense and homogenous structures (98 % of the theoretical density [32]).

2.3. Actuator and harvester, measurement and simulation

A critical point in MEMS sensor and actuators is represented by the deposition and patterning of crystalline piezoelectric materials which limit the possibility of fabricating complex actuator or sensor structures exploiting piezoelectricity. To exploit the advantages of 3D printing piezoelectric materials, we printed micrometric active and passive device to demonstrate the possibility of fabricating in one step piezo MEMS with complex geometries. Clamped-clamped beams (namely "bridges") and circular membranes are fabricated by printing approach with micrometric resolution, completely composed of polycrystalline Barium Titanate. These two basic MEMS structures were chosen for their amplification of the mechanical movement towards the center of the devices which facilitate the experimental measurements. After electrode deposition, the devices are tested to work both as passive device like a vibration sensor or a mechanical energy harvester and as active device like a microactuator.

The functionality like passive device as sensor or energy harvester is evaluated by mounting the piezoelectric MEMS with an adhesive tape on an electromechanical actuator to undergo mechanical stimuli (scheme in Fig. 2a). In this configuration, the device is exposed to an external mechanical stimulus, which generates an electrical signal due to the piezoelectric properties of the ceramic material. The electrical signal corresponds to the mechanical stimulus in both amplitude and frequency, allowing the piezoelectric device to sense vibrational signals without requiring an external power source. Additionally, the material's ability to convert mechanical deformation into electrical energy can be harnessed to harvest wasted mechanical energy, which can be directly used or stored in a storage device. In this study, the passive device, represented by a suspended clamped–clamped beam with 1.6 mm length, 300 μm width and 60 μm thickness (Fig. 2b), is subjected to mechanical stimuli with the same deformation amplitude in the range between 5 Hz and 100 kHz to evaluate the frequency response of the piezo MEMS. Mechanical stimuli were given to the whole piezoelectric structure in the shape of sinusoidal, triangular and square mechanical vibration while the voltage generated at the two end of the suspended piezo bridge are measured. In Fig. 2d–f presents the voltage generated in the MEMS when subjected to sinusoidal deformation at 10 Hz, 500 Hz and 100 kHz. Maximum amplitude for each frequency and phase of generated signal with respect to the stimulus one are shown in Fig. 2c. 3D printed piezo bridge is able to generate an electrical voltage that follow the shape of the mechanical stimulus demonstrating its feasibility as vibrational sensor. The generated voltage output increases while rising the excitation frequency up to 500 Hz, while it decreases after this value. At the same time the phase difference between input and output signal is changing from around 90° to −65° with a variation of almost 180° and phase 0° at 500 Hz. Both amplitude and phase of the generated signal evidence the presence of an electrical resonance of the piezoelectric device around 500 Hz which would represents the frequency from which it is possible to reach the higher voltage generation with the same external signal amplitude. The mechanical resonance is at higher frequency, as will be shown later. A similar behavior is also reported with a mechanical stimulus with triangular shape (see Fig. 2g and Fig. S5), even if the output signals have slight shape distortion with respect of the actuation signal because of the difficulty of the samples to mechanically follow abrupt change of direction. This effect is more evident with square actuation signal where the outputs at low frequency have a high voltage increases when the mechanical square signal is rising or falling and then it exponentially decreases (see Fig. S6). This phenomenon is also due to charge recombination and screening in piezoelectric materials which prevents them to use as static strain/pressure sensors, because they cannot detect a time prolongated mechanical deformation. The presence of these voltage spikes give rise to a high peak-to-peak voltage generation with low frequency square actuation (Fig. 2g), even if the effective generated charges are small because of the short time duration of the spikes.

These measurements demonstrate the capability of the 3D printed devices to generate electrical voltage under mechanical stimuli. Printed device could work as vibration sensor to detect frequency and amplitude of an external mechanical stimulus without the need of power supply. Direct piezoelectric effect could be exploited not only for sensing, but also for harvesting mechanical energy converting into electrical energy. This capability of 3D printed BTO device was demonstrated by connecting the bridge device to a capacitor in order to store the generated electrical charges upon periodic mechanical stimulus. Since the electrical signal generated by the piezo device is both positive and negative, a bridge rectifier was used to harvest all the bridge output as schematized in Fig. 2h (inset). The BTO bridge demonstrate its potential application as energy harvester by rapidly charge a 33 μF capacitor when subjected to sinusoidal deformation at 500 Hz. Using the same mechanical stimulus of Fig. 2h the capacitor reach a maximum value of 5 V in around 10 s. Lower voltage and longer duration are reached by decreasing the amplitude of the mechanical stimulus.

Exploiting indirect piezoelectric effect, 3D printed devices could be used as microactuactor with the possibility of controlling the mechanical movements in the nanometric scale. Microactuators are devices that produce mechanical displacement in the nano or micrometer range when subjected to an input signal. Piezoelectric microactuators utilize the inverse piezoelectric effect to deform mechanically in response to an electrical stimulus. Since the mechanical deformation is proportional to the input signal, it is possible to control the actuator with high precision in both time and amplitude. Printed devices were connected to a signal generator coupled with a voltage amplifier to send the electrical actuation signal. Device deformations were evaluated with a laser doppler vibrometer with sub-picometer resolution (scheme of measurement set-up shown in Fig. 3a). A bridge and a membrane (3 mm diameter and 200 μm thickness) devices were tested as actuators. Both device showed

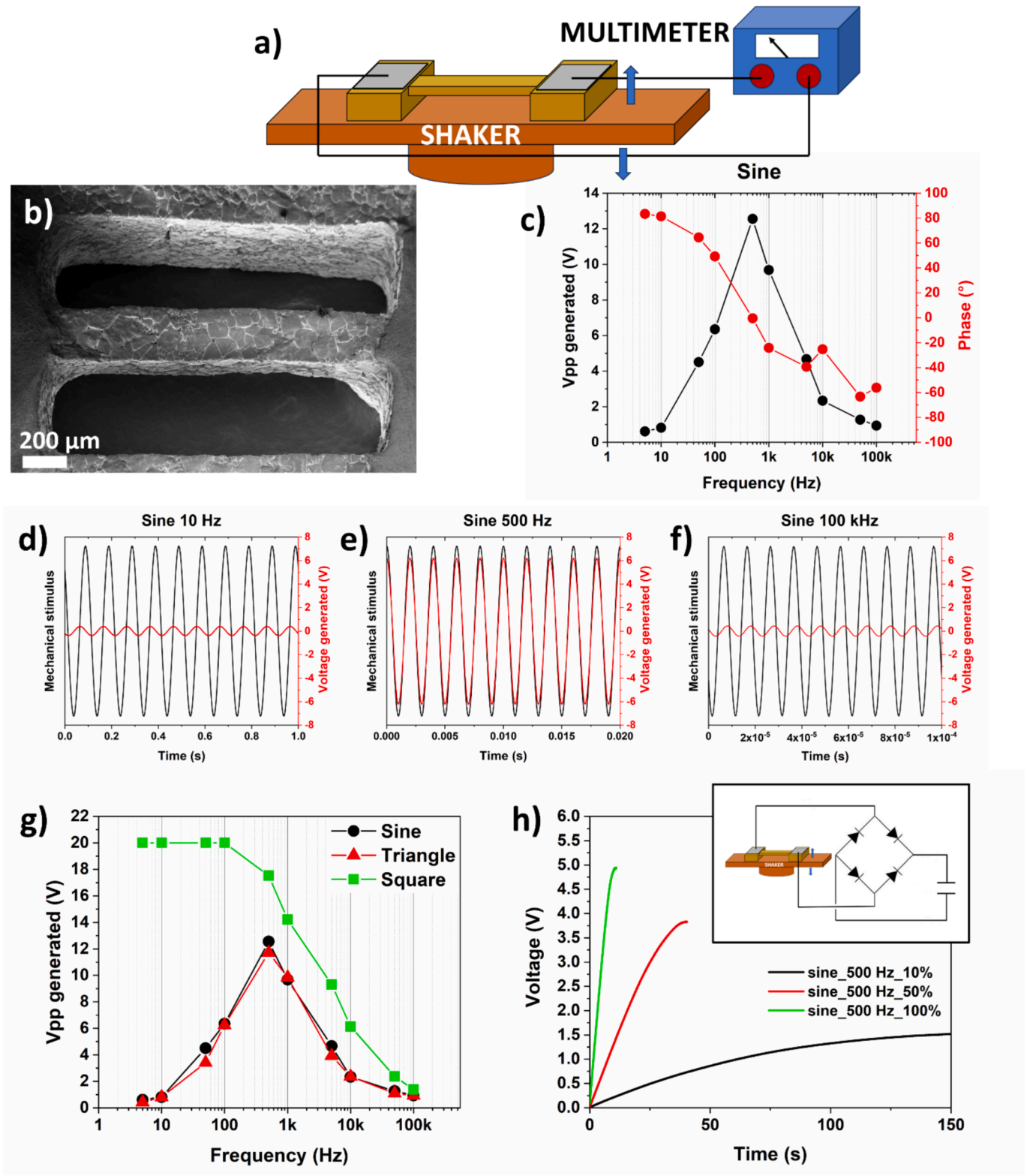

Fig. 2. a) Schematic of the direct measurement set-up of a 3D printed barium titanate bridge. b) SEM image of the printed device. at the sides of the bridge is visible the silver paste used for electrical contact. scale bar corresponds to 200 µm. c) Peak-to-peak amplitude and phase of the voltage generated by the 3D printed bridge under sinusoidal mechanical stimuli at different frequencies. Electrical voltage output of the BTO bridge when subjected to a mechanical sinusoidal stimulus at frequency of d) 10 Hz, e) 500 Hz and f) 100 kHz. g) Peak-to-peak amplitude of the voltage generated by the 3D printed bridge under sinusoidal, triangular and squared mechanical stimuli at different frequencies. h) Charging of 33 µF capacitor during mechanical stimulation at 500 Hz of BTO bridge with different oscillation amplitude with respect of stimulus of e). The inset shows the equivalent circuit scheme of the piezo device coupled to the capacitor with a rectifier bridge.

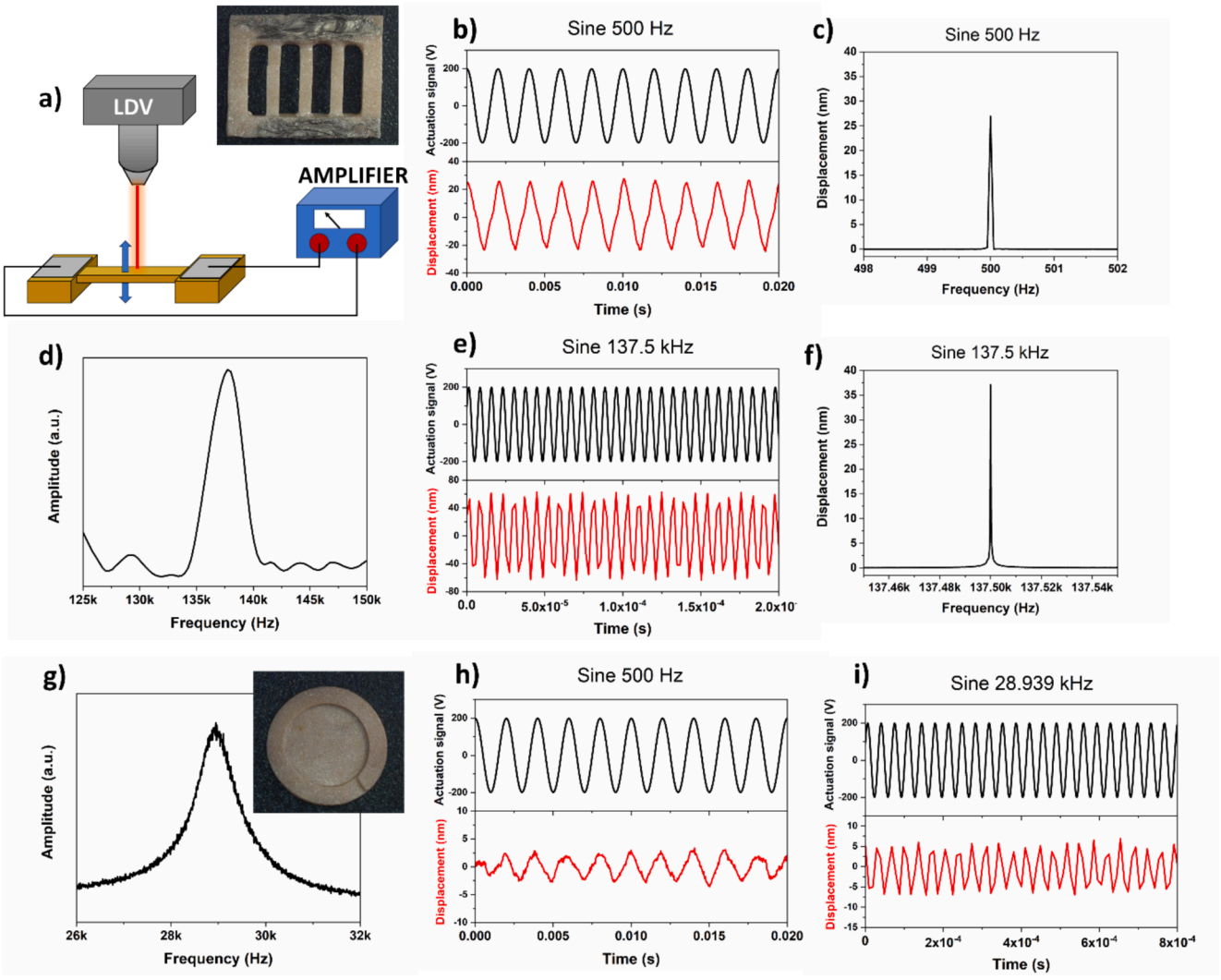

Fig. 3. a) Schematic of the indirect measurement set-up of a 3D printed barium titanate bridge. image of the printed device in the inset. b) Sinusoidal voltage actuation signal at frequency of 500 Hz (black) and induced displacement (red) of the center of the bridge. c) FFT of bridge displacement signal under 500 Hz sinusoidal actuation. d) Amplitude spectrum of printed bridge device showing first mode mechanical resonance frequency peak centered around 137.5 kHz. e) Sinusoidal voltage actuation signal at frequency of 137.5 kHz (black) and induced displacement (red) of the center of the bridge. f) FFT of bridge displacement signal under 137.5 kHz sinusoidal actuation. g) Amplitude spectrum of 3D printed BTO membrane device showing first mode mechanical resonance frequency peak centered around 28.939 kHz. Image of the printed device in the inset. Sinusoidal voltage actuation signal at frequency of h) 500 Hz and i) 28.939 kHz and related induced displacement of the center of the membrane. (For interpretation of the references to colour in this figure legend, the reader is referred to the web version of this article.)

the ability to follow the actuation signal when electrically stimulated with an electrical sinusoidal signal at frequency of 500 Hz (around piezoelectric resonance of the device) and peak amplitude of 200 V (Fig. 3b and h). Fast Fourier Transform (FFT) of the displacement signal confirms that the displacement of the devices is peaked on the actuation frequency with a very low frequency broadening (Fig. 3c and Fig. S7a). Bridge device had higher mechanical displacement with respect of membrane one (27 nm vs 1.8 nm), since the structure is less constrained because of only two opposite clamping in contrast to an all-around clamping for the membrane sample. The device can also be controlled with electrical signal with different shape, as demonstrated with the 3D printed bridge structure with square and triangular signal with frequency of 500 Hz and peak amplitude of 200 V (Figs. S8 and S9). High displacement was obtained for both device around electrical resonances, but a way to increase the mechanical displacement of the actuator device is working around mechanical resonance. Investigation of the resonance frequency was performed by actuating the devices with a sweep signal in a large frequency bandwidth and measuring the vibration amplitude of the sample. From frequency peaks in the FFT of the measured signals, resonance frequencies of 137.5 kHz (Fig. 3d) and 28.939 kHz (Fig. 3g) were found for bridge and membrane actuator, respectively. Using these values, both the actuators were stimulated with an actuation signal centered at their resonance frequencies (Fig. 3e and i), obtaining a much higher deformation with respect of 500 Hz actuation (37.1 nm for bridge and 6.2 nm for membrane). Mechanicaly induced deformation was still well peaked around actuation frequency as reported in the FFT plots (Fig. 3f and Fig. S7b). The higher actuation response at mechanical resonances is fundamental to build efficient actuators. Indeed mechanical resonance frequency can be tuned by changing device geometry, easily obtainable with a 3D printing fabrication technique, tailoring the device response depending on the specific application.

2.4. Complex 3D printed object

3D printing technology allows higher degree of freedom in the design

of new devices, also for piezoelectric materials. To fully exploit these potentialities we design a metamaterial piezoelectric structures taking inspiration from the research work of Cui *et al.* that printed the structures made of composite organic–inorganic materials with a specially designed printer [29]. In our study, the piezoelectric structure is fully ceramic, and composed of a cubic lattice formed by repetition of a single cell unit to form a trabecular structured (Fig. 4a–c). This complex 3D structures was designed to increase the local stress in the structures during the application of a load, increasing the piezoelectric output with respect of a bulky device. To test the enhanced piezoelectric responses of the designed metamaterials structure, we design an experiment applying different forces by dropping balance calibration weights ranging from 1 g to 50 g were sequentially dropped from an height of 5 cm on the 3D printed BTO trabecular structure and on a bulky one with the same dimensions. Finite Element Method (FEM) simulations were performed to evaluate the different response in terms of electrical output of the two piezoelectric structures to a pulsed force applied on the top surface. Both generated structures are deformed under the applied force and generate an electrical output pulse signal in time. From the simulation, the metamaterial device is expected to generate a 6.5 times higher voltage response with respect of the bulk structures (Fig. 4d and e). Experimental tests conducted on both geometries show that the mechanical stress induced by the impact generates an electrical voltage output of the piezoelectric device proportional to the calibration weight (Fig. 4f). Fig. 4g shows that the generated voltage linearly increase with the magnitude of the impact weight both for metamaterial structure and for the bulk one. As expected from the simulation, the BTO trabecular structure, designed to enhance the piezoelectric response, shows an increase of the generated voltage. Experimentally, the output voltage exhibits a four time enhancement for the metamaterial structure compared to the bulk, lower than the simulated one. This discrepancy can be ascribed to a lower polarization of the horizontal rods of the structures during the poling process and to the higher number of defects and lower dimension of the piezoelectric grains in the metamaterial structures with respect of the printed bulk one because of the small dimension of the cell unit components, both conditions that could not be taken into account during the simulation. Anyway these results demonstrated that our 3D printing approach of piezoelectric device can be exploited to fabricate complex device with enhanced performances with respect of standard fabrication processes. The 3D metamaterial structure can find application also to recover mechanical energy from human movement, converting in electrical energy. An example is reported in Fig. 4h and i where, upon periodic compression with fingertip (like during a keyboard typing), 3D printed device generates a voltage and current signal upon each compression (positive signal) and release (negative signal) with the finger. The generated electrical signal remains stable in

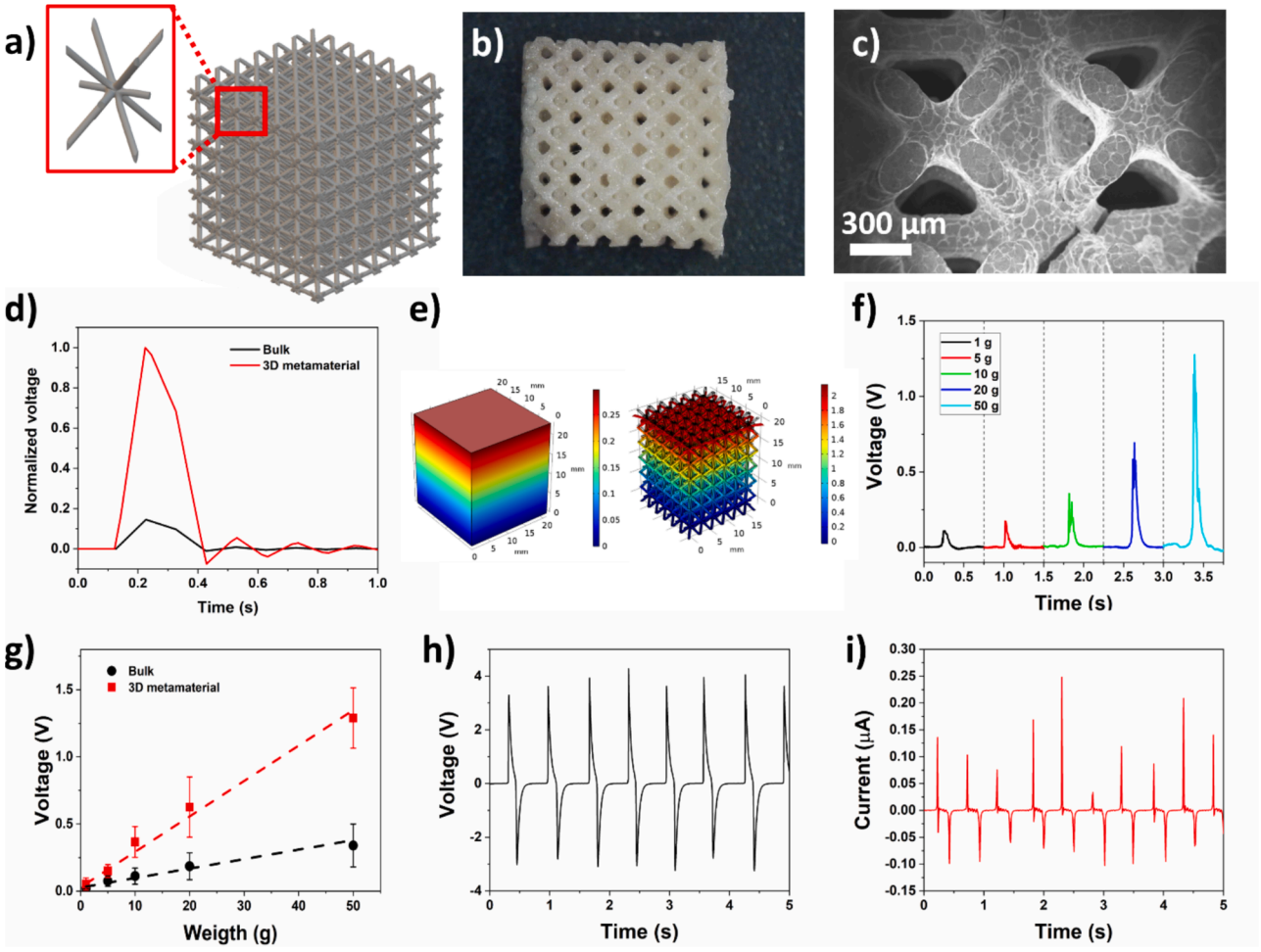

Fig. 4. a) CAD files of the single unit cell and the whole piezoelectric metamaterial structure. b) Image of the 3D printed metamaterial structure. c) SEM images showing details of the bto printed structure. Scale bar corresponds to 300 µm. d) Simulated electrical output of printed bulk and metamaterial structures when subjected to a pulsed force on the top surface. e) FEM simulations of electrical output of bulky and 3D metamaterial BTO structure. f) Electrical voltage signal generated upon impact of different balance calibration weights falling from an height of 5 cm on the metamaterial device. g) Voltage generated upon impact of different weights on the metamaterial and on the bulk printed structures. Error bars refer to the standard deviation of at least 20 different measurements. h) Electrical voltage and i) current generated upon periodic compression with fingertip on the 3D printed BTO metamaterial structure.

time (with variation related to different force applied by fingertip) evidencing the stability under mechanical cyclic stress of the metamaterial structures (Fig. S10). The electrical output signal can be used to charge a capacitor (upon signal rectification) demonstrating the device ability as energy harvester (Fig. S11).

3. Conclusion

In our study, we present a novel approach to fabricate lead-free piezoelectric complex structures using additive manufacturing technologies. Traditional 3D printing of piezoelectric ceramic materials relies on a slurry containing inorganic micro and nanoparticles dispersed in a polymeric matrix. However, this composition often proves too viscous for easy printing and, in the case of additive manufacturing based on photocurable resin, leads to significant light scattering, reducing spatial resolution. To overcome these challenges, we have developed particle-free piezoelectric inks based on sol–gel processes. By employing Digital Light Processing technology, we successfully fabricated highly dense and homogeneous piezoelectric structures. The barium titanate structures printed through this method exhibit a piezoelectric coefficient of 50 pm/V. This breakthrough allows us to showcase the potential of our approach in creating intricate 3D MEMS devices entirely composed of active materials. We have validated the printed micrometric clamped–clamped beams and membranes as both active devices for use as actuators and passive devices for applications such as displacement sensors and energy harvesters. Furthermore, our flexibility in device fabrication enables to print 3D metamaterial piezoelectric structures designed to concentrate mechanical stress during force application, thereby enhancing the electrical response compared to bulk structures. These particle-free techniques for 3D printed piezoelectric devices address the complexities associated with preparing microstructured active and passive devices using standard lithographic techniques. For future research, improving of the piezoelectric performance can be obtained by changing the sintering conditions to have a control over the crystals size, optimizing poling process in terms of temperature and electric field, improving electrical coupling between ceramic and electrodes by silver firing approach or doping barium titanate with materials such calcium and strontium. In conclusion, our work opens the door to the creation of innovative sensors, actuators, and harvesters, leveraging the design freedom offered by additive manufacturing technology.

4. Materials and methods

4.1. Materials

The following materials were used without further purification: Barium acetate (ACROS Organics, ACS reagent, 99+%), acetic acid (ACROS Organics, 99.8 %), titanium (IV) isopropoxide (TTIP, Sigma-Aldrich, ≥97.0 %), acrylic acid (Sigma-Aldrich, anhydrous, containing 200 ppm MEHQ as an inhibitor, 99 %), ethoxylated (15) trimethylolpropane triacrylate (SR9035, SARTOMER), 2,4,6-trimethylbenzoyldiphenylphosphineoxide (TPO, Irgacure), Sudan orange G (Reidel-de Haen).

4.2. Barium titanate ink preparation

The preparation of the BTO ink has been optimized in our previous work [31]. To prepare 100 g ink, the preparation procedure is as follows: Initially, 24.05 g barium acetate was dissolved in a solution containing 3.79 g acetic acid and 1.25 g double-distilled water (DW) at 65 °C, within a PET vial. The resulting solution was then cooled to room temperature (RT). TTIP 26.75 g was mixed in another PET vial with 2.99 g acetic acid, under gentle stirring. Subsequently, the barium acetate solution was poured into the TTIP solution under vigorous stirring, followed by a 7-minute low-power sonication bath.

At the next stage, 0.45 g DW was added to this mixture under vigorous stirring. After 10 min, 3.55 g acrylic acid was added, and 15 min later, 2.60 g SR9035 was added. The resulting composition was shielded from light exposure by wrapping the PET vial with an aluminum foil. Following this, 0.60 g TPO was introduced into the reaction mixture, and a subsequent 3-minute sonication process in a cleaning bath was performed.

4.3. Printing and post-printing

The printing process was performed using a DLP 3D printer (MAX, Asiga). This printer utilizes a UV-LED light source (405 nm) with an intensity of 23.5 mW/cm^2. For each layer, the exposure time was fixed at 3 s, and the layer thickness was 50–200 μm.

The printed objects were rinsed with technical isopropanol to remove uncured ink from within the printed structures. Then, the objects were aged for two weeks in a closed small cap to ensure slow evaporation in order to prevent cracks. Following aging, the samples were heated under air in a tube oven (Zhengzhou Kejia Furnace, China). The heating profile was as follows: The samples were heated or cooled at a rate of 2.5 °C/min. The temperature was held for one hour after reaching each of the following temperatures: 90, 250, 385, 655, 900,1430 and 1300 °C in this order, and then cooled down to room temperature. The thermal process was performed while the printed objects were placed in an alumina crucible boat, filled with zirconia beads to enable homogenous shrinkage of the structures.

4.4. Material and device characterizations

XRD evaluation was done with X-Ray Powder Diffractometer D8 Advance (Bruker AXS). Device dimension measurements and energy dispersive X-ray (EDX) analysis are performed with a Zeiss MERLIN field emission scanning electron microscope.

Before piezoelectric and functional characterization, electrodes were prepared by using silver paint on the surfaces of the devices. Each sample was the poled in silicon oil (80 °C) under an high voltage electric field of 6 kV/cm for 4 h. Then, still applying the electric field, the device was naturally cool down to room temperature [39].

Current–voltage (I–V) curves, ferroelectric polarization hysteresis loops, and piezoelectric displacement measurements were recorded simultaneously by a Piezo Evaluation System (PES, TFAnalyzer 2000HS, Aixacct) coupled to a single point laser vibrometer (Polytec OVF-505), exploiting the converse piezoelectric effect (i.e., generation of a mechanical displacement under the application of an electric field).

Measurement of device as actuator or harvester were performed with a Laser Doppler Vibrometer (LDV MSA-500, Polytec Gmbh) coupled with a lock-in amplifier (UHFLI, Zurich instruments) to evaluate device mechanical displacement and electrical output. Voltage signal for device actuation, generated by LDV system, was amplified by means of a high-voltage amplifier (A400, Pendulum). Electrical voltage and current signal generated upon weight impact and fingertip pressing were measured by a high impedance electrometer (Keithley 6517b, Tektronix).

CRediT authorship contribution statement

Tamar Rosental: Writing – original draft, Investigation, Data curation, Conceptualization. **Gabriele Gatani:** Software. **Candido Fabrizio Pirri:** Writing – review & editing, Supervision, Resources. **Carlo Ricciardi:** Writing – review & editing, Validation, Supervision, Methodology. **Daria Savraeva:** Data curation, Investigation. **Ayelet Bunin:** Data curation, Investigation. **May Yam Moshkovitz-Douvdevany:** Data curation, Methodology. **Shlomo Magdassi:** Writing – review & editing, Validation, Supervision, Resources, Conceptualization. **Stefano Stassi:** Writing – review & editing, Writing – original draft, Investigation, Data curation, Conceptualization.

Declaration of competing interest

The authors declare that they have no known competing financial interests or personal relationships that could have appeared to influence the work reported in this paper.

Data availability

Data will be made available on request.

Acknowledgements

This research was supported by the Ministero dell'Università e della Ricerca (MUR), through PRIN 2022 – PASSO Prot. 20222TKNRJ grant. The generous support of Ms. Susan Lawi for the scholarship of TR via the American Friends of The Hebrew University is highly appreciated.

Appendix A. Supplementary data

Supplementary data to this article can be found online at https://doi.org/10.1016/j.cej.2024.156189.

References

[1] K. Zhang, G. Gao, C. Zhao, Y. Wang, Y. Wang, J. Li, Ultrason. Sonochem. 96 (2023) 106438.
[2] L. Jiang, Y. Yang, R. Chen, G. Lu, R. Li, D. Li, M.S. Humayun, K.K. Shung, J. Zhu, Y. Chen, Q. Zhou, Nano Energy 56 (2019) 216.
[3] N. Sezer, M. Koç, Nano Energy 80 (2021) 105567.
[4] M. Hassanpour Amiri, R. Fatscher, R. Taylor, P.R.F. Rocha, C.R. Bowen, K. Asadi, Nano Energy 106 (2023) 108073.
[5] M. Laurenti, M. Fontana, S. Stassi, A. Sacco, A. Scalia, S. Bianco, C.F. Pirri, A. Lamberti, Adv. Mater. Interfaces 10 (2023) 2300485.
[6] C. Shao, Y. Zhao, L. Qu, SusMat 2 (2022) 142.
[7] Y.-G. Kim, J.-H. Song, S. Hong, S.-H. Ahn, NPJ Flexible Electron. 6 (2022) 52.
[8] M. Schlögl, J. Weißenbach, M. Schneider, U. Schmid, Sens. Actuators A: Phys. 349 (2023) 114067.
[9] A. Tommasi, G. Coletta, D. Balma, S.L. Marasso, D. Perrone, G. Canavese, S. Stassi, S. Bianco, M. Cocuzza, C.F. Pirri, Microelectron. Eng. 119 (2014) 137.
[10] J. Toledo, V. Ruiz-Díez, A. Diaz-Molina, D. Ruiz, A. Donoso, J.C. Bellido, E. Wistrela, M. Kucera, U. Schmid, J. Hernando-García, J.L. Sánchez-Rojas, Actuators 6 (2017) 19.
[11] M.S. Mirza, Q. Liu, T. Yasin, X. Qi, J.-F. Li, M. Ikram, Ceram. Int. 42 (2016) 10745.
[12] Z. Mirzazadeh, Z. Sherafat, E. Bagherzadeh, Ceram. Int. 47 (2021) 6211.
[13] H. Liu, Y. Gao, S. Ding, F. Peng, D. Zhu, Int. J. Adv. Manuf. Technol. 100 (2019) 251.
[14] V. Cauda, B. Torre, A. Falqui, G. Canavese, S. Stassi, T. Bein, M. Pizzi, Chem. Mater. 24 (2012) 4215.
[15] G. Canavese, S. Stassi, V. Cauda, A. Verna, P. Motto, A. Chiodoni, S.L. Marasso, D. Demarchi, IEEE Sens. J. 13 (2237) (2013) 6468056.
[16] X. Liu, Y. Shang, J. Zhang, C. Zhang, ACS Appl. Mater. Interfaces 13 (2021) 14334.
[17] Y. Zeng, L. Jiang, Q. He, R. Wodnicki, Y. Yang, Y. Chen, Q. Zhou, J. Phys. D: Appl. Phys. 55 (2022) 013002.
[18] S. Bodkhe, P. Ermanni, Multifunctional Mater. 2 (2019) 022001.
[19] C. Chen, X. Wang, Y. Wang, D. Yang, F. Yao, W. Zhang, B. Wang, G.A. Sewvandi, D. Yang, D. Hu, Adv. Funct. Mater. 30 (2020) 2005141.
[20] M. Bach, T. Sebastian, M. Melnykowycz, T. Lusiola, D. Scharf, F. Clemens, presented at Industrializing Additive Manufacturing – Proceedings of Additive Manufacturing in Products and Applications – AMPA2017, Cham, 2018, 2018.
[21] H. Kim, T. Fernando, M. Li, Y. Lin, T.-L.-B. Tseng, J. Compos. Mater. 52 (2017) 197.
[22] B. Nan, S. Olhero, R. Pinho, P.M. Vilarinho, T.W. Button, J.M.F. Ferreira, J. Am. Ceram. Soc. 102 (2019) 3191.
[23] X. Liu, J. Liu, L. He, Y. Shang, C. Zhang, Adv. Funct. Mater. 32 (2022) 2201274.
[24] Y. Yang, S. Peng, F. Qi, J. Zan, G. Liu, Z. Zhao, C. Shuai, Mater. Sci. Eng. C 116 (2020) 111195.
[25] Z. Chen, X. Song, L. Lei, X. Chen, C. Fei, C.T. Chiu, X. Qian, T. Ma, Y. Yang, K. Shung, Y. Chen, Q. Zhou, Nano Energy 27 (2016) 78.
[26] W. Chen, F. Wang, K. Yan, Y. Zhang, D. Wu, Ceram. Int. 45 (2019) 4880.
[27] D. Zhang, Y. Yang, W.-F. Rao, Micromachines 14 (2023) 1146.
[28] S.-M. Chang, S. Hur, J. Park, D.-G. Lee, J. Shin, H.S. Kim, S.E. Song, J.M. Baik, M. Kim, H.-C. Song, C.-Y. Kang, Addit. Manuf. 67 (2023) 103470.
[29] H. Cui, R. Hensleigh, D. Yao, D. Maurya, P. Kumar, M.G. Kang, S. Priya, X. Zheng, Nat. Mater. 18 (2019) 234.
[30] S. Liu, W. Wang, W. Xu, L. Liu, W. Zhang, K. Song, X. Chen, Research (2022) 2022.
[31] S. Stassi, I. Cooperstein, M. Tortello, C.F. Pirri, S. Magdassi, C. Ricciardi, Nat. Commun. 12 (2021) 6080.
[32] T. Rosental, S. Mizrahi, A. Kamyshny, S. Magdassi, Virtual Phys. Prototyping 16 (2021) 255.
[33] A. Mayeen, K.M. S, M.S. Jayalakshmy, S. Thomas, D. Rouxel, J. Philip, R.N. Bhowmik, N. Kalarikkal, Dalton Trans. 47 (2018) 2039.
[34] H. Pei, J. Jing, Y. Chen, J. Guo, N. Chen, Nano Energy 109 (2023) 108303.
[35] V. Cauda, S. Stassi, K. Bejtka, G. Canavese, ACS Appl. Mater. Interfaces 5 (2013) 6430.
[36] S. Bodkhe, G. Turcot, F.P. Gosselin, D. Therriault, ACS Appl. Mater. Interfaces 9 (2017) 20833.
[37] S.M. Gaytan, M.A. Cadena, H. Karim, D. Delfin, Y. Lin, D. Espalin, E. MacDonald, R. B. Wicker, Ceram. Int. 41 (2015) 6610.
[38] C. Chen, X. Wang, Y. Wang, H. Gu, W. Zhao, W. Zhang, G.A. Sewvandi, B. Wang, C. Ma, M. Liu, D. Hu, Adv. Compos. Hybrid Mater. 6 (2023) 41.
[39] X. Wei, Y. Liu, D. Zhao, S.S. Ge, J. Eur. Ceram. Soc. 40 (2020) 5423.